Optical Investigation of the Influence of In-cylinder Flow and Mixture Inhomogeneity on Cyclic Variability in a Direct-Injection Spark Ignition Engine

Judith Laichter[1] · Sebastian A. Kaiser[1]

Abstract

In this study, a single-cylinder direct-injection spark-ignition research engine with full optical access was used to investigate the influence of the flow field and fuel/air mixing on cyclic variability, in particular in the early flame propagation. The engine was operated under lean-burn conditions at 1500 rpm. Two different injection strategies were compared, port-fuel injection (PFI) and direct injection (DI), the latter with early and late injection split about 2:1 in fuel mass. High-speed particle image velocimetry captured the flow in the tumble plane in the compression stroke. The velocity fields and the movement of the tumble vortex are analyzed. Simultaneously, a second camera detected the chemiluminescence of the flame, and the projected area of the line-of-sight-integrated flame luminosity was extracted through morphological image processing. By combining pressure-based combustion analysis and high-speed optical diagnostics, the early flame propagation and the flow field are correlated. In separate experiments the equivalence ratio was imaged for the DI at selected crank angles and correlated with CA10 to learn about the influence of mixture inhomogeneity on early flame propagation. With PFI, the flow near the spark plug just before ignition is closely related to the subsequent speed of combustion. The combustion-relevant flow features can be traced back in time to about –90 °CA. In contrast, the chosen DI scheme results in a decorrelation of flow and flame, and the equivalence ratio distribution at ignition becomes more important. For both flow and mixture fields, regions of high correlation with early-combustion metrics are typically associated with gradients in the multi-cycle average fields.

✉ Judith Laichter
judith.laichter@uni-due.de

Sebastian A. Kaiser
sebastian.kaiser@uni-due.de

[1] Institut für Verbrennung und Gasdynamik, Universität Duisburg-Essen, Carl-Benz-Straße 199, 47057 Duisburg, Germany

1 Introduction

Direct-injection spark-ignition (DISI) engines are a fuel–saving alternative to homoge-nously premixed-charge engines with port-fuel injection. However, they suffer from their increased sensitivity to cycle-to-cycle variations (CCV) (Anderson et al. 1996; Fansler et al. 2015). The stability of the cycle is particularly affected by the early phase of com-bustion, which is strongly correlated with the initial growth of the flame kernel (Aleiferis et al. 2004; Mansour et al. 2008; Ozdor et al. 1994). Previous experimental investigations have therefore focused on investigating the region near the spark plug during ignition and early flame propagation (Aleiferis et al. 2000, 2004; Peterson et al. 2014). In the work of Aleiferis et al. (Aleiferis et al. 2004) the early flame kernel was investigated and a strong correlation between the crank angle at which 10% of the fuel mass are burned (CA10) and the equivalent flame radius was identified. They also investigated the connection between flame growth and convection. They found that the flame grows faster when the convection velocity in the swirl and tumble planes is higher during the first crank angles after ignition, corresponding to 0.1–1% mass fraction burned. Another example of connecting the early flame with more global pressure-based metrics Hanushkin et al. (Hanuschkin et al. 2020), who applied machine learning methods to predict the cycles with high maximum in-cylin-der peak pressure based on optical cross-sections of the flame shortly after ignition timing.

The rotating movement of the in-cylinder charge, the tumble flow, influences the early flame kernel growth and is known to be one origin of CCV (Peterson et al. 2011; Bode et al. 2017; Heywood 2018) (p. 450–453). This tumble flow becomes unstable towards firing top dead center (TDC), and the kinetic energy of large scales of the flow is transferred into small-scale turbulence. Direct injection adds significant momentum to the flow, and if that injection is scheduled late, large velocity gradients may still be present at ignition. A key technique for gaining insight into the pre-ignition flow is high-speed particle image velocimetry (PIV), which provides crank-angle resolved flow fields in a two-dimensional plane (Fajardo and Sick 2007; Müller et al. 2010; Peterson and Sick 2010). Measurements with high-speed PIV in an optically accessible DISI engine found the center position of large-scale tumble vortex varied substantially in the horizontal direction, while the vertical direction was mainly determined by the piston movement (Müller et al. 2010). Another PIV study (Buschbeck et al. 2012) with lean operation revealed that the variation of the kinetic energy has a relatively small influence on CCV compared to the dominant large-scale flow structures.

With late injection, significant mixture inhomogeneity (so-called "stratification") can be expected at ignition timing. The spatial distribution of the fuel is usually assessed from laser-induced fluorescence imaging of a "tracer" added to the non-fluorescing surrogate fuel (Einecke et al. 2000). Combining LIF and PIV, Peterson et al. (Peterson et al. 2014, 2011) conducted a multiparameter analysis simultaneously capturing the flow field, mix-ture field, and early flame development for stratified combustion, with a focus on one of the extremes of CCV—misfires. A key finding was that misfires did not result from failure to ignite, but from failure to enflame. The spark always developed into an early flame kernel, but for unfavorable combinations of flow and fuel concentration fields it extinguished soon after and was not able to enflame the entire charge. While misfires are a particular prob-lem in spray-guided operating strategies, where the injection is in close spatio-temporal proximity to the spark, they are much less of an issue when the injection is earlier, as it is more commonly implemented in commercial engines. Nevertheless, also in such less extreme cases it is of general practical and fundamental interest to understand how flow and mixing influence CCV and what methods can be used to track these influences back
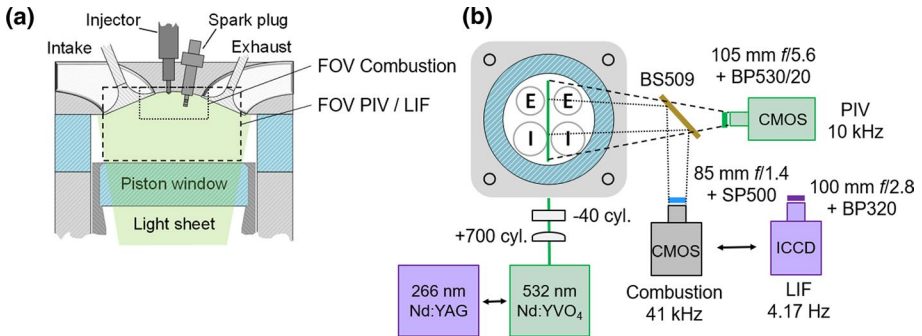
Fig. 1 Sketches of **(a)** optical engine with the fields-of-view of the two measurements and **(b)** imaging optics

Table 1 Engine operating conditions

	PFI	DI
Bore x stroke	84 mm × 90 mm	
Compression ratio	9:1	
Engine speed	1500 rpm	
Fuel	98% iso-octane + 2% anisole	
Spark timing	−20°CA	
Equivalence ratio Φ	0.91	
Intake temperature	55°C	
Intake pressure	1 bar	1.1 bar
Injection timing	–	−330°CA / −56°CA
Injected fuel mass	24 mg	21.6 mg / 10 mg
IMEP	7.7 bar	7.8 bar
COV of IMEP	1%	4%

in time towards their sources. To this end, we here combined pressure-trace analysis with combustion luminosity, LIF, and PIV imaging. From a base case with PFI, a case with direct injection was examined using two main tools, conditional averaging of slow and fast-burning cycles, and field-wide correlation analysis. The latter technique had been applied to flow-spray interaction in a DISI engine (Stiehl et al. 2016) and is expanded here to track the influence of flow and mixing from ignition back in time.

2 Optical Engine and Operating Conditions

The experiments were performed in an optically accessible four-stroke single-cylinder DISI engine. Fig. 1 shows an illustration of engine and optics, and Table 1 summarizes the operating conditions. The engine was operated at 1500 rpm, and two different injection strategies were applied. The first operating point (OP) with port-fuel injection (PFI) serves as a homogenous reference case. For the second OP (DI) a double injection was implemented using the centrally located 8-hole "Spray G" injector of the international

research collaboration "Engine Combustion Network" (ECN). 70% of the fuel are injected at −330°CA[1] and the remaining 30% of the fuel are injected 56°CA before compression top dead center (TDC). The second injection was approximately at "Spray G standard" conditions (here, the core gas temperature and density were 238°C and 3.5 kg/m^3, respectively). To reach this condition, the intake pressure was increased to 1.1 bar, which slightly influences the pressure traces during the compression stroke and results in a higher intake air mass flow but is not expected to influence the flow field. The latter is considered by also increasing the injected fuel mass, so that the global air–fuel ratio remained the same. With $\Phi = 0.91$, the mixture was relatively lean, resulting in a coefficient of variation (COV) of the indicated mean effective pressure (IMEP) of 1 and 4% for PFI and DI, respectively. We note that DI strategy was not optimized towards a "useful" cycle outcome, like low COV or high IMEP, but designed to have higher COV than with PFI while still never misfiring.

To minimize the thermal load and the potential influence of residual gas on CCV, each fired cycle was followed by two motored cycles. With DI, fuel was injected only in the fired cycles, while with PFI, every cycle was fueled. For this reason, the global equivalence ratio of the operating point with DI is corrected by the residual gas fraction, which is estimated here to be 10% based on the compression ratio.

The high-speed imaging of flow field and flame and the "low-speed" (crank-angle locked) imaging of the equivalence ratio Φ were conducted in separate experiments. Flow fields and flame propagation were captured simultaneously. Because of the limited image storage capacity of the camera, three measurement series were performed at the same operating condition with short interruptions in between. These three image series from 71 fired cycles were combined into a data set of 213 cycles for each OP. In separate experiments the equivalence ratio Φ for DI was imaged at three selected crank angles (−60, −35 and −20°CA). Here, two series of 100 fired cycles were combined to a set of 200 for each crank angle. A piezoelectric pressure sensor measured the in-cylinder pressure, and the pressure traces were used to calculate the heat release rate, the IMEP, and its COV in both experiments.

2.1 Optical Diagnostics

Optical access is given by a fused-silica cylinder liner and a flat piston window. For PIV, a frequency-doubled, single-cavity Nd:YVO$_4$ laser (Edgewave IS335, 532 nm, 1 mJ/pulse) was operated with 20 µs between the pulses illuminating two related images. In the combustion chamber the vertical 0.6 mm thick laser sheet illuminated the central tumble plane. Silicon oil droplets (~ 1 µm diameter) were seeded 50 cm upstream into the intake. A CMOS camera (Photron SA-Z) with a 105 mm lens at f/5.6 captured the light scattered by the silicon oil droplets, operating at 20 kHz (i.e., image pairs were acquired at 10 kHz). PIV imaging started at −180°CA and continued to ignition timing. Due to the high intensity of the scattered light from the second injection in DI useful vector fields could not be calculated between –56 and –36°CA. Simultaneously, another CMOS camera (Phantom v7.3) with an 85 mm lens at f/1.4 imaged line-of-sight integrated blue combustion luminosity at a frame rate of 41 kHz. This chemiluminescence imaging started at –29°CA and

---

[1] This paper assigns 0°CA to compression top-dead center, i.e., crank angles during intake and compression are negative.

ended 5°CA after TDC. Images that are taken before the spark event are used for background correction.

For the equivalence ratio Φ, laser pulses from a frequency-quadrupled Nd:YAG laser at 266 nm were formed to a light sheet and directed into the combustion chamber illuminating the same central tumble plane as in the PIV measurements. The fluorescence signal from 2% anisole (methoxybenzene) dissolved in the iso-octane fuel was captured by an intensified CCD camera (LaVision IRO) with a 100 mm f/2.8 UV lens. 2×2 pixel hardware binning was set. The gate was set to 150 ns, and the gain was 65 (as set in the control software DaVis). One image was acquired at a selected crank angle in each fired cycle. To block scattered laser light and to detect only the part of the anisole fluorescence spectrum with lower temperature sensitivity (Kranz et al. 2018) (Fig. 4) a 40 nm-wide bandpass filter centered at 320 nm (Semrock) was used. The pulse energy was about 20 mJ/pulse. All cameras' approximate fields of view (FOV) are shown in Fig. 1.

2.2 Data Processing

PIV vector calculation was done with LaVision's DaVis 8.4. In pre-processing, to eliminate background such as from laser light reflections, a Butterworth high-pass time filtered image (7 images time window) was subtracted from each raw image. Also, a sliding background subtraction (100×100 pixel) and a local intensity normalization (5×5 pixel) were used. For vector calculation, a multi-pass cross-correlation with the window size decreasing from 64×64 to 32×32 pixels with an overlap of 50% was applied and vectors with a peak ratio < 1.3 were removed. This resulted in a vector spacing of 914 μm.

To extract spatial information from the chemiluminescence images, a global region of interest was defined by masking out the cylinder roof and the border regions. An average background of 30 dark images in each cycle before the spark event was subtracted from the flame images, and a 5×5 pixel median filter reduced pattern and shot noise. The apparent burnt area of size A_{flame} was extracted using a "predictor–corrector scheme" that segments the image using a dynamically adjusted intensity threshold (Shawal et al. 2016). From that, the equivalent flame radius calculated as $r_{flame} = (A_{flame}/\pi)^{1/2}$ (Aleiferis et al. 2000).

For the LIF images IDI the images IPFI of the homogenous PFI reference case serve as calibrating "flat fields" while cycles without fuel injection provided background images I_{BG}. Dividing the background-corrected single shots by the average flat field and multiplying it with the global equivalence ratio of PFI yields the equivalence ratio images $I_{\Phi, DI}$:

$$I_{\Phi,DI} = \frac{I_{DI} - <I_{BG}>}{\left(<I_{PFI}> - <I_{BG}>\right)} \Phi_{PFI}, \tag{1}$$

where bold font indicates two-dimensional image quantities and < > multi-cycle averaging. The global temperature and pressure dependency of anisole fluorescence is taken into account by recording the PFI calibration images under the same conditions and at the same crank-angle as with DI. The influence of local deviations in temperature associated with the local (inhomogeneous) equivalence ratio is minimized by detecting only the longer-wavelength part of the anisole fluorescence. Experiments with the same filter as used here (Semrock 320/40) showed that with air as the bath gas, the LIF signal detected at 650 K varies only 10% for a variation of 100 K (Kranz et al. 2018).

To identify regions in the flow or mixture field that are correlated with a measure of combustion speed (early flame propagation or CA10), "correlation maps" were created,

Fig. 2 Equivalent flame radius at −9°CA vs. CA10 for all cycles in both OPs
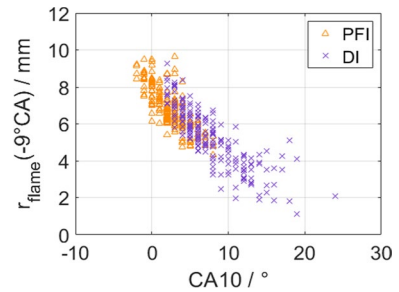
as suggested by, e.g., (Stiehl et al. 2016). The idea behind correlation maps is to look how well some single-value quantity correlates with a scalar field quantity at any point in a two-dimensional field. Here, the equivalent flame radius 11°CA after ignition timing [$r_{flame}(-9°CA)$] was correlated with the velocity magnitude $|v|$, and CA10 was correlated with the equivalence ratio Φ. The correlation coefficient $R_{x,y}$ is defined as.

$$R_{x,y} = \frac{\sum_{i=1}^{n}(x_i - \bar{x})(y_i - \bar{y})}{\sqrt{\sum_{i=1}^{n}(x_i - \bar{x})^2 \sum_{i=1}^{n}(y_i - \bar{y})^2}} \tag{2}$$

with $x = |v|$ or Φ, and $y = r_{flame}(-9°CA)$ or CA10. This results in two time series of correlation maps. The correlation coefficient varies between -1 and 1, where $|R_{x,y}| < 0.3$ implies a low degree, $0.3 < |R_{x,y}| < 0.5$ some degree, $0.5 < |R_{x,y}| < 0.7$ a significant degree, and $|R_{x,y}| > 0.7$ a high degree of dependence (Holický 2013) (p. 142–144).

3 Results

We first examine the correlation of flame imaging and pressure-trace analysis. A scatterplot of the equivalent flame radius at –9°CA (11°CA AIT) versus CA10 is shown in Fig. 2. The correlation value for PFI and DI is 0.77, and 0.83 respectively—both indicating a strong correlation. This means that cycles can be classified as 'slow' or 'fast' based on either the imaging data or the classic pressure-trace metrics, but the former provides an earlier indication of the cycle outcome than the latter, qualitatively confirming one of the central findings of Aleiferis et al. (Aleiferis et al. 2004, 2000).

Figure 3 gives more detailed information on the spatio-temporal characteristics of flame propagation. Here, the probability of finding burnt area in a given pixel is shown as the mean over the 35 fastest and the 35 slowest cycles, based on their CA10. The figure also shows the centroid position of the burnt area in each cycle. For both OPs in fast cycles the flame spreads randomly around the spark plug, yielding a round to oval area of high probability without a clear outer edge. In slow PFI cycles the apparent burnt area remains near the spark plug and slightly moves towards the intake valve. In contrast, for slow DI cycles the flame spreads towards the exhaust side. The fast PFI cycles are faster than the fast ones with DI, and the same is true for each OP's slow subset. In slow PFI cycles the flame has a circular shape, while in slow DI cycles it is more an oval. Comparing the fast and the slow PFI cycles across crank angles with approximately equal flame extent, for example fast at −13°CA vs. slow at −8.8°CA, we see that the flame centroids are further apart for the fast cycles, consistent with the more random spread of the flame diagnosed above. To
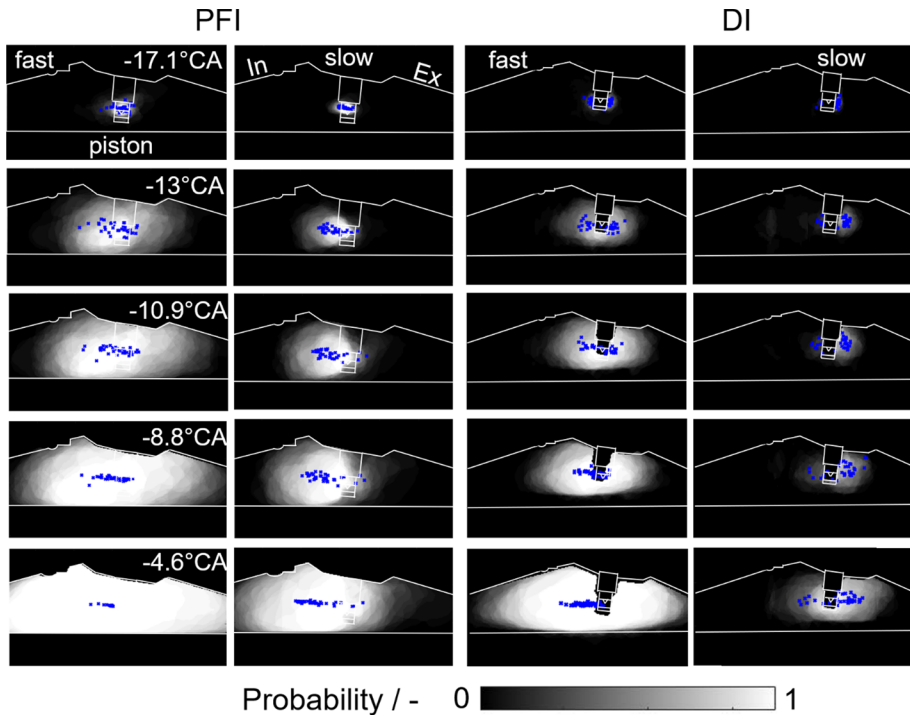
Fig. 3 Mean probability of finding burnt area at a given location for the 35 fastest ('fast') and 35 slowest ('slow') cycles (by CA10) during early flame propagation. The blue markers indicate the centroid position of each cycle's burnt area

see what might cause all these differences, we next examine the in-cylinder flow preceding combustion.

In Fig. 4 the velocity fields conditionally averaged over the fast cycles and slow cycles are shown. For PFI throughout most of the FOV, the flow at −90°CA is faster in the slow cycles than in the fast ones. From −45°CA on, the inverse is true — now for PFI the fast burning cycles also have the faster mean flow. This is consistent with the notion that it is the kinetic energy late in the cycle, towards combustion, that matters for turbulent flame propagation. We also see a marked difference for slow vs. fast cycles developing in the location of the tumble vortex. The vortex center in slow cycles moves towards the exhaust side but remains in the center in fast ones. In general, towards TDC the round shape of the tumble vortex is not compliant with the increasingly vertically constrained geometry of the combustion chamber. This vertical compression creates shear and breaks up the vortex (Borée et al. 2002). Since the pent-roof has most headroom in the center, a vortex local-ized there can keep its momentum longer, transferring its large-scale energy later into tur-bulence. Another flow feature in the PFI case that is visible after –45°CA is a region of strong "sweeping" flow above the piston, directed upward and towards the intake. Here, the velocity is higher for fast cycles than slow cycles. This flow feature appears to arise from the combination of the centrally located vortex and the upward movement of the piston. The standard deviation at −19.8°CA is low in this region between spark plug and piston top, which means that the flow is quite stable here. In comparison to that, in both fast and
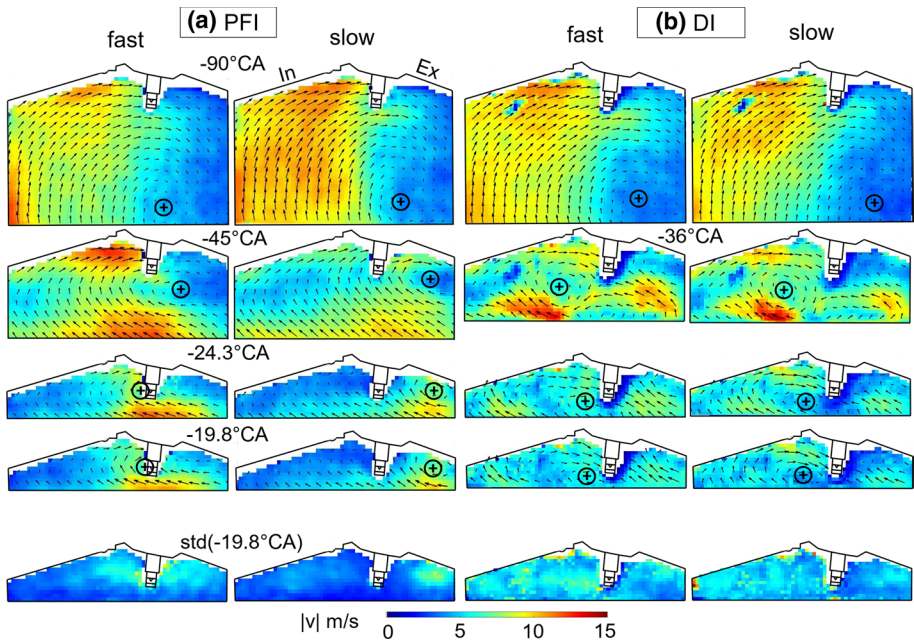
Fig. 4 Selected mean velocity fields for the 35 fastest and 35 slowest cycles (by CA10) for **(a)** PFI and **(b)** DI. For DI, due to the spray of the second injection the vectors fields at −45°CA are highly inaccurate, and the first reliable flow field after the injection (at −36°CA) is shown instead. The black + marker indicates the visually determined center of the tumble vortex. The last row shows the standard deviation of the velocity magnitude across each data sub-set at −19.8°CA

slow cycles the region where the vortex center is located has a higher standard deviation, indicating that small deviations in the vortex location cause high variations near its center, but less farther away from it.

At –90°CA, i.e., before the second injection, DI is very similar to PFI, indicating that the first injection that occurred at –330°CA during the intake stroke had little influence on the in-cylinder flow during compression. (Note that in DI the small region with near-zero velocities below the intake valve and that on the right side of the spark plug are due to reflections in the background and should be ignored.) But in DI at – 36 °CA the second injection has taken place shortly before, and it has a significant impact on the flow field. It adds additional turbulence and makes the flow more three-dimensional, which cannot be captured completely in only one imaging plane. However, a vortex is still visible on the intake side next to the spark plug. The orientation of the vectors is almost identical in fast and slow cycles, but almost everywhere, fast cycles have slightly higher velocity magnitudes. As in PFI, the vortex in DI is squeezed by the piston movement during compression. At − 24.3 °CA the vortex center is less pronounced in DI than in PFI, which can have two reasons. Either the two-dimensional plane does not capture the vortex anymore or the vortex starts to dissipate earlier. The standard deviation at ignition (−19.8°CA) is higher for fast cycles than for slow cycles, is overall higher for DI than for PFI, and reaches its peak on the intake side next to the spark plug. A visual inspection of the single-cycle flow fields (not shown here) reveals that with DI the vortex has mostly dissipated, while with PFI a more coherent flow remains. The direction of the vectors in DI at –20°CA is still the same

for fast and slow cycles. However, the slow cycles have higher velocities on the intake side of the spark plug, directed towards the exhaust side, while in fast cycles there is a local counter-flow with similar velocity magnitudes on both sides.

The flow behavior at ignition timing is linked with subsequent flame propagation (Fig. 3). As noted above, with PFI at −19.8°CA the vortex center is associated with a region of elevated standard deviation in velocity magnitude, but in fast cycles, this region is exactly around the spark plug. The associated cycle-to-cycle variation in the vortex center's location exposes the spark to different flow directions. For example, if the vortex center is located on the intake side and below the spark plug, the spark is carried to the intake side, while the opposite is the case when the center is located on the exhaust side. The varying location of the vortex center for fast cycles is therefore very likely to be the reason for the variation in the location of the burnt area. Conversely, if the vortex center is always on the same side of the spark plug, like in the slow cycles of PFI, the flow always convects the flame to the same side, even when the location of the vortex slightly varies.

In DI, at ignition (−20°CA) the flow in slow cycles has a higher velocity magnitude on the intake side of the spark plug than the counter-flow on the opposite side of the spark plug. This flow behavior results in a movement of the flame to the exhaust. In contrast, the velocity magnitude in fast cycles is approximately the same on both sides of the spark plug, which may lead to the observed spreading in the flame probability.

To better link the flame and flow data, correlation maps were created (based on all 213 cycles for each OP). Figure 5 shows the correlation of the vector magnitude $|v|$ with the equivalent flame radius at –9°CA. Any correlation can now be traced back in time, and in fact Fig. 5 has been arranged in reverse temporal order to facilitate that narration.

First, we look at PFI as the base case. A patch of strong correlation around the spark plug can be seen at ignition timing (−20°CA). Looking back in time, this region is expanding until –40°CA without decreasing in the correlation coefficient. Interestingly, the vortex center is surrounded by a ring of high correlation coefficients where the gradient between near-zero mean flow at the vortex center and the faster flow around it is located. Also, from ignition back to –50°CA the sweeping flow above the piston and below the spark plug shows a high correlation. This region may disappear with the piston top from the field of view at earlier CAD. Peterson et al. (2019) also found a correlation between the upward-sweeping flow in this region and combustion. At –50°CA the patch of high correlation near the spark plug and around the vortex center slightly decreases and start to split up into several smaller regions. Going now backwards in time the region of higher correlation below the inlet slowly decreases towards –90°CA until it is not visible anymore. However, the region immediately to the left of the tumble vortex center increases in spatial extent and magnitude. Again, it is not at the vortex center that the highest correlation is found, but next to it. Comparing the correlation maps at −40 (or −50) and –90 °CA with the conditional averages in Fig. 4 we see that these high-correlation areas are exactly where the differences in flow magnitude between slow and fast cycles are found.

Compared to PFI, DI almost always has much lower correlation coefficients. From −20 to –36 °CA several higher-correlation patches are located roughly around the vortex center. This is consistent with the lack of cylinder-wide coherent flow that we in turn ascribe to the second injection at –56°CA, but also with the fact that with DI a second parameter of influence appears, namely mixture inhomogeneity, which will be assessed in the next section. However, at −60 and –75 °CA (before the second injection) there is a relatively large region in the center of the FOV where higher correlation coefficients occur. This is somewhat surprising but may be due to the three dimensional nature of the flow that is captured only partially by the current planar PIV measurement or due to a causal chain between

Fig. 5 Correlation maps of the velocity magnitude with the equivalent flame radius at −9°CA
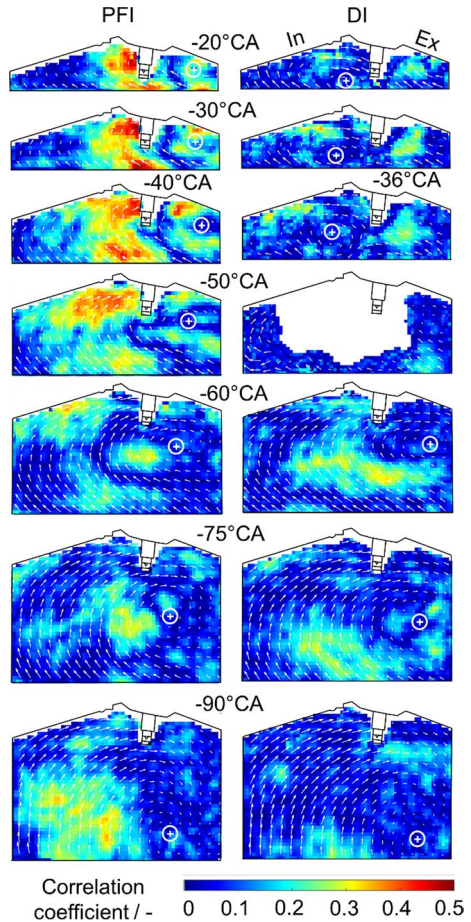
flow–spray–flame, i.e., the pre-injection flow influences the spray and thereby the mixture formation and finally the flame (Stiehl et al. 2016). At –90°CA the correlation value has decreased below 0.2.

These correlation maps illuminate the causal chain between flame and large-scale flow as they are able to identify regions that are likely to influence the early flame kernel growth with PFI. However, with DI the second injection suddenly inserts smaller-scale turbulence, and moreover it may stratify the mixture to an extent where the flow is not the dominating influence on the flame propagation anymore. Therefore, for the DI case we next look at the local equivalence ratio Φ.

For the DI case, Fig. 6a shows conditional 'fast' and 'slow' 35-cycle averages of the equivalence ratio and typical corresponding single shots. The near vertical "stripes" in the images stem from shot-to-shot fluctuations in the transverse laser beam profile. They have a modulation of about 6% (one standard deviation) which should not preclude reaching qualitatively meaningful conclusions. The images at –60°CA show that, as intended, the first injection at –330°CA generates an almost homogenous, globally lean mixture. However, there is a leaner region above the piston, slightly more so for fast cycles than for slow ones. The single shots show the corresponding gradients better. It seems that in this
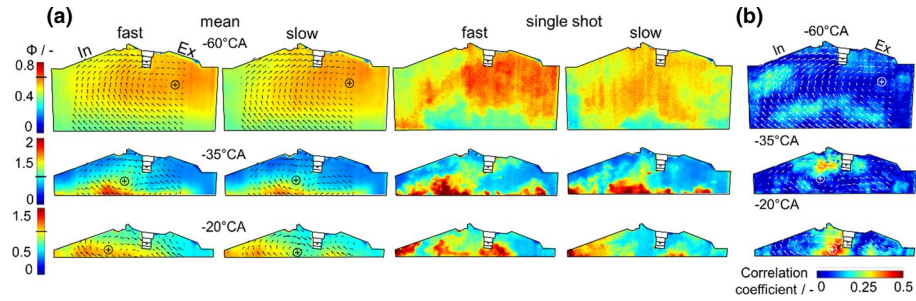
Fig. 6 **(a)** Equivalence ratio at selected crank angles. First and second column: Conditional average over the 35 fastest and 35 slowest cycles superimposed by the averaged flow fields from Fig. 4. Third and fourth column: corresponding typical single shots selected from each 35-image subset. **(b)** Correlation maps of the equivalence ratio and CA10 superimposed with the average flow field from Fig. 4

mixture before the second injection, a typical fast cycle has more stratification than a slow cycle.

The second injection introduces much stronger mixture inhomogeneity. At −35°CA most of the fuel is still close to the piston top for both fast and slow cycles. At ignition timing (−20°CA) in slow cycles the fuel is concentrated more at the intake side and a leaner region is found around the spark plug. Fast cycles also have more fuel on the intake side, but the richer region it is horizontally extended and the equivalence ratio around the spark plug is approximately 1. This would lead to better conditions for the early flame kernel. The flame imaging summarized in Fig. 3 showed that slow cycles burn towards the right, and the flow fields in Fig. 4 indicated that this is partly because in slow cycles the generally right-ward flow near the spark plug is stronger. We now additionally see that for fast cycles the immediate vicinity of the spark has better mixture conditions to the left of the spark plug, which may make it easier for the flame to propagate left against convection.

In Fig. 6b the correlation between the equivalence ratio in each pixel and CA10 is shown. As expected, at ignition timing there is a strong correlation around the spark plug. In particular the region on the intake (left) side has more influence on CA10 than on the exhaust side, where the correlation coefficient is almost zero. This is consistent with the earlier conclusion that fast cycles occur when the early kernel can expand against the flow to the left. Earlier in time at –35°CA the region of stronger correlation remains but decreases in value. The small spots of low correlation stem from liquid fuel droplets that saturate the camera sensor. At –60°CA, before the second injection, the correlation coefficient is much lower. However, what little correlation exists is found in the regions where significant gradients are seen in the equivalence ratio in Fig. 6a.

4 Conclusions

This work used several optical imaging techniques to investigate cyclic variability in the early flame for gasoline port-fuel injection (PFI) and central direct injection (DI) with moderate fuel inhomogeneity at ignition. The latter used a split injection that delivered about one-third of the fuel late at −56°CA. Two main tools were used in the analysis, averaging of the image data conditional on cycles being among the 35 fastest or slowest burning ones, and correlation maps that quantify how well a single-value quantity

correlates with a scalar field quantity at any point in a two-dimensional field. Both were found to yield useful and complementary insights.

In flame luminosity imaging, for PFI slow cycles are more likely to burn towards the intake side of the spark plug, but for DI, to the exhaust side. For both PFI and DI in fast cycles the location of the flame varies much more, but on average is more centered around the spark plug.

In flow fields from PIV, with PFI the vortex center in slow cycles moves horizontally towards the exhaust side of the combustion chamber, whereas the vortex center in fast cycles remains more in the center, which appears to help maintain higher bulk flow velocities until closer to TDC. The second injection in DI changes the flow field completely. Afterwards, for both fast and slow cycles the vortex center is found on the intake side of the spark plug.

Correlation maps of the velocity magnitude with the equivalent flame radius at –9°CA were analyzed. For PFI, the maps reveal large regions that predict the speed of the combustion process, in particular below the center of the pent-roof and an upward "sweeping" flow above the piston. Some of these regions can be traced back in time to about –90°CA. The second injection of DI results in a different location of the relevant region, and with lower correlation coefficient. In all cases regions of high correlation with the early flame do not coincide with the tumble vortex center, but are instead adjacent, sometimes arranged in a loose circular pattern around it. High-correlation areas are where the greatest differences in flow magnitude between slow and fast cycles are found.

For DI, the equivalence ratio was measured with tracer LIF and then correlated with CA10. After the second injection, regions of high correlation are to the immediate left of the spark plug, where in fast cycles a distinct gradient towards a fuel-rich zone is found, but not in slow ones. This is upstream against the local flow, suggesting that the mixture gradient enables the flame to burn against local convection, enlarging the region that is "available" for the early kernel. As a result, the flame is then found (in the combustion images) with more equal likelihood everywhere around the spark plug.

Declarations

Conflict of interest The authors declare that they have no conflicts of interest.

References

Aleiferis, P.G., Taylor, A.M.K.P., Whitelaw, J.H., Ishii, K., Urata, Y.: Cyclic variations of initial flame kernel growth in a honda VTEC-E lean-burn spark-ignition engine. SAE Technical Paper 2000-01-1207 (2000)

Aleiferis, P.G., Taylor, A., Ishii, K., Urata, Y.: The nature of early flame development in a lean-burn stratified-charge spark-ignition engine. Combust Flame **136**, 283–302 (2004)

Anderson, W., Yang, J., Brehob, D.D., Vallance, J.K., Whiteaker, R.M.: Understanding the thermodynamics of direct injection spark ignition (DISI) combustion systems: an analytical and experimental investigation. SAE Technical Paper 1996-10-01 (1996)

Bode, J., Schorr, J., Krüger, C., Dreizler, A., Böhm, B.: Influence of three-dimensional in-cylinder flows on cycle-to-cycle variations in a fired stratified DISI engine measured by time-resolved dual-plane PIV. Proc. Combust. Inst. **36**, 3477–3485 (2017)

Borée, J., Maurel, S., Bazile, R.: Disruption of a compressed vortex. Phys. Fluids **14**, 2543 (2002)

Buschbeck, M., Bittner, N., Halfmann, T., Arndt, S.: Dependence of combustion dynamics in a gasoline engine upon the in-cylinder flow field, determined by high-speed PIV. Exp Fluids. **53**, 1701–1712 (2012)

Einecke, S., Schulz, C., Sick, V.: Measurement of temperature, fuel concentration and equivalence ratio fields using tracer LIF in IC engine combustion. Appl. Phys. B **71**, 717–723 (2000)

Fajardo, C., Sick, V.: Flow field assessment in a fired spray-guided spark-ignition direct-injection engine based on UV particle image velocimetry with sub crank angle resolution. Proc. Combust. Inst. **31**, 3023–3031 (2007)

Fansler, T.D., Reuss, D.L., Sick, V., Dahms, R.N.: Invited Review: combustion instability in spray-guided stratified-charge engines: a review. Int. J. Engine Res. **16**, 260–305 (2015)

Hanuschkin, A., Zündorf, S., Schmidt, M., Welch, C., Schorr, J., Peters, S., Dreizler, A., Böhm, B.: Investigation of cycle-to-cycle variations in a spark-ignition engine based on a machine learning analysis of the early flame kernel. Proc. Combust. Inst. **38**, 5751–5759 (2020)

Heywood, J.B.: Internal Combustion Engine Fundamentals. McGraw-Hill, New York (2018)

Holický, M.: Introduction to Probability and Statistics for Engineers, 1st edn. Springer, Berlin (2013)

Kranz, P., Fuhrmann, D., Goschütz, M., Kaiser, S. A., Bauke, S., Golibrzuch, K., Peter,W., Julian, K., Lars, L., Jasper, B., Manuel, Z., Olaf, S., Berg, T. T.: In-Cylinder LIF Imaging IR-Absorption Point Measurements and a CFD Simulation to Evaluate Mixture Formation in a CNG-Fueled Engine. SAE Int. J. Engine **11**(6), 1221–1238. https://doi.org/10.4271/2018-01-0633 (2018)

Mansour, M., Peters, N., Schrader, L.-U.: Experimental study of turbulent flame kernel propagation. Exp. Therm. Fluid Sci. **32**, 1396–1404 (2008)

Müller, S.H.R., Böhm, B., Gleißner, M., Grzeszik, R., Arndt, S., Dreizler, A.: Flow field measurements in an optically accessible, direct-injection spray-guided internal combustion engine using high-speed PIV. Exp Fluids. **48**, 281–290 (2010)

Ozdor, N., Dulger, M., Sher, E.: Cyclic variability in spark ignition engines a literature survey. SAE Technical Paper 940987 (1994)

Peterson, B., Sick, V.: High-speed flow and fuel imaging study of available spark energy in a spray-guided direct-injection engine and implications on misfires. Int. J. Engine Res. **11**, 313–329 (2010)

Peterson, B., Reuss, D.L., Sick, V.: High-speed imaging analysis of misfires in a spray-guided direct injection engine. Proc. Combust. Inst. **33**, 3089–3096 (2011)

Peterson, B., Reuss, D.L., Sick, V.: On the ignition and flame development in a spray-guided direct-injection spark-ignition engine. Combust Flame **161**, 240–255 (2014)

Peterson, B., Baum, E., Dreizler, A., Böhm, B.: An experimental study of the detailed flame transport in a SI engine using simultaneous dual-plane OH-LIF and stereoscopic PIV. Combust. Flame **202**, 16–32. https://doi.org/10.1016/j.combustflame.2018.12.024 (2019)

Shawal, S., Goschutz, M., Schild, M., Kaiser, S., Neurohr, M., Pfeil, J., Koch, T.: High-speed imaging of early flame growth in spark-ignited engines using different imaging systems via endoscopic and full optical access. SAE Int J Engines **9**, 704–718 (2016)

Stiehl, R., Bode, J., Schorr, J., Krüger, C., Dreizler, A., Böhm, B.: Influence of intake geometry variations on in-cylinder flow and flow–spray interactions in a stratified direct-injection spark-ignition engine captured by time-resolved particle image velocimetry. Int. J. Engine Res. **17**, 983–997 (2016)